Rheological Modeling of Carbon Nanotube Suspensions with Rod–Rod Interactions

G. Natale, M. C. Heuzey, and P. J. Carreau
Center for Applied Research on Polymers and Composites (CREPEC), Chemical Engineering Dept., École Polytechnique de Montréal, PO Box 6079, Stn Centre-Ville, Montreal, QC, Canada H3C3A7

G. Ausias and J. Férec
Laboratoire d'Ingénierie des MATériaux de Bretagne (LIMATB), Université Européenne de Bretagne, rue de St Maudé, 56325 Lorient, France

DOI 10.1002/aic.14316
Published online December 30, 2013 in Wiley Online Library (wileyonlinelibrary.com)

To explain the shear-thinning behavior of untreated carbon nanotube (CNT) suspensions in a Newtonian matrix, a new set of rheological equations is developed. The CNTs are modeled as rigid rods dispersed in a Newtonian matrix and the evolution of the system is controlled by hydrodynamic and rod–rod interactions. The particle–particle interactions is modeled by a nonlinear lubrication force, function of the relative velocity at the contact point, and weighted by the contact probability. The stress tensor is calculated from the known fourth-order orientation tensor and a new fourth-order interaction tensor. The Fokker-Planck equation is numerically solved for steady simple shear flows using a finite volume method. The model predictions show a good agreement with the steady shear data of CNTs dispersed in a Newtonian epoxy matrix as well as for suspensions of glass fibers in polybutene,[1] demonstrating its ability to describe the behavior of micro- and nanoscale particle suspensions. © 2013 American Institute of Chemical Engineers *AIChE J*, 60: 1476–1487, 2014

Keywords: Modeling of suspensions, carbon nanotubes (CNTs), interaction tensors, Fokker-Planck equation, steady shear flow, shear thinning behavior

Introduction

The popularity of carbon nanotubes (CNTs) as polymer fillers can be easily understood considering the high-added value achievable for creating multifunctional composites. However, an essential requirement for CNT success in potential applications is a clear understanding and control of material properties' evolution during flow and processing. Hence, the rheology of CNT suspensions has been intensely investigated in the last few decades by different authors.[2–6]

CNTs dispersed in a matrix form complex microstructures due to their high-aspect ratio, and van der Waals forces. The microstructure is a function of CNT concentration, aspect ratio and dispersion, and it evolves with and without flow with corresponding changes in the rheological properties.[2,4,7,8] Many rheological studies have been published on the linear viscoelastic behavior and on the nonterminal character (in percolated systems) of the storage modulus and complex viscosity at low frequencies, considered as the rheological signature of an established filler network.[6,8,9] In addition, small amplitude oscillatory shear (SAOS) measurements have been used as an indirect method to characterize the suspension, correlating mixing time, dispersion state and network elasticity.[3]

The nanotubes form an elastic network with a characteristic shear modulus and yield stress, both of which increase with CNT concentration.[5,10] The network structure is very sensitive and it can be easily destroyed by steady shear and large amplitude oscillatory shear (LAOS) deformation. However, the microstructure keeps evolving under quiescent conditions and a network reorganization takes place, as illustrated by the behavior of the stress overshoot in reverse flow as function of rest time[6,11] or by the storage modulus as function of time.[12]

Direct and indirect rheo-optical studies have shown evidences that the anisotropy is enhanced with increasing shear rate and/or volume fraction, due to rotational excluded-volume interactions.[13–15] Mechanical interlock of the nanotubes caused by inter-particle collisions in confined geometry was also shown by Ma et al.[16] Another unique rheological characteristic is the shear-thinning behavior of CNT-based suspensions, even when the carbon nanotubes are added to a Newtonian matrix. The viscosity at low shear rates can be several orders of magnitude higher than that of the neat medium, while it tends to level off asymptotically toward that of the latter at high shear rates.[17] There is not a univocal explanation for this shear-thinning phenomenon, but shear thinning seems to be due to a combination of nanotube orientation and agglomerates breakup.

Correspondence concerning this article should be addressed to P. J. Carreau at pcarreau@polymtl.ca.

To entirely characterize such a complex system, it is necessary to grasp the interplay between the different mechanisms that control the evolution of the microstructure such as hydrodynamic forces, Brownian motion, attractive forces and particle interactions. Modeling is a powerful tool to understand the causes behind the microstructure evolution and, thus, can open new routes to specifically develop enhanced composite properties and processing schemes.

The first successful attempt to model anisotropic particles was achieved by Jeffery.[18] In his work, he described the orientation evolution of a single spheroid in a Newtonian medium in the absence of Brownian motion and particle interactions. He showed that a particle rotates around the vorticity axis and remains in the same orbit forever. However, most of the real suspensions (blood, composites, paints) contain many particles and direct and indirect interactions play a major role in their rheological properties. Models have been developed based on the presence of hydrodynamic interactions.[19,20] Hydrodynamic interactions happen when a particle is in the vicinity of a second particle, causing disturbances in the flow field as seen by the second particle. This introduces fluctuations in the orbits before steady-state is reached.

Later, Petrich et al.[21] showed experimentally that particle interactions becomes more and more important as the particle concentration increased, but the hydrodynamic theories were not able to capture the enhancement in viscosity and first normal stress difference. An original approach aimed at including these effects was proposed by Folgar and Tucker[22] and Advani and Tucker,[23] introducing an empirical diffusional term into the Jeffery equation

$$\dot{\mathbf{p}} = -\frac{1}{2}\boldsymbol{\omega}\cdot\mathbf{p} + \frac{1}{2}\lambda(\dot{\boldsymbol{\gamma}}\cdot\mathbf{p} - \dot{\boldsymbol{\gamma}} : \mathbf{ppp}) - C_I|\dot{\gamma}|\frac{\partial \ln(\psi)}{\partial \mathbf{p}}, \quad (1)$$

where $\mathbf{p}$ is the unit vector directed along the particle principal axis, $\boldsymbol{\omega}$ and $\dot{\boldsymbol{\gamma}}$ are the vorticity and deformation rate tensors, respectively, and the shape factor $\lambda = (r^2-1)/(r^2+1)$ is a parameter related to the particle aspect ratio $r = L/D$. The phenomenological term (last term in Eq. 1) is proportional to the effective deformation rate $|\dot{\gamma}| = \sqrt{\dot{\boldsymbol{\gamma}} : \dot{\boldsymbol{\gamma}}/2}$ and to a constant diffusion coefficient C_I. Several authors have proposed formulations for the diffusion coefficient as function of fiber aspect ratio and volume fraction.[24–26]

Recently, Ma et al.[27] showed that a Fokker-Planck advection-diffusion description, with a constant rotary diffusion, failed to capture the experimentally observed rheological responses of untreated CNT suspensions. They proposed an innovative approach named the "aggregation/orientation" (AO) model that takes into account the different possible microstructures in a CNT suspension, but its predictions were limited to low CNT volume fractions and different adjustable parameters were needed for each concentration. Following this trend, Chinesta[28] proposed a realistic model based on a double-scale kinetics theory, considering at a first scale the kinematics of the clusters and at a second one, the kinematics of the rods constituting the clusters.

A more complete theory for concentrated rodlike suspensions with strong particle interactions was presented by Sandstrom and Tucker.[29,30] They modeled the interparticle contacts as a linear lubrication force. This work was extended by Servais et al.[31,32] assuming that in addition to the lubrication force at each contact point there were a Coulombic friction force and a normal force of elastostatic origin. Furthermore, Djalili-Moghaddam and Toll[33] proposed a nonlinear formulation of the model and considered the total stress as the sum of the contributions of the matrix, hydrodynamic forces and interaction forces. However, only short-range hydrodynamic interactions were taken into account. Finally, Férec et al.[34] generalized their work, not neglecting any term in the particle relative velocity expression, and constructed a new conformation tensor called the interaction tensor.

A different approach was undertaken by Le Corre et al.[35] based on a deterministic upscaling technique to establish the fundamental properties of the macroscopic mechanical behavior of planar distributed fiber networks, and it was later extended for the case of high concentrated fiber bundle suspensions dispersed in a non-Newtonian power-law fluid.[36] The shear-thinning behavior was also considered by Guiraud et al.[37] to evaluate the average contact force, and in addition to the approach of Servais et al.,[31] two new aspects were examined (1) the dependence of contact surfaces on fiber bundle orientation, and (2) the influence of the confining pressure.

The aforementioned approaches have an important point in common: they provide a description of the suspension system at a mesoscopic scale where the microstructure is defined by a distribution function that depends on time, physical space and chosen conformational coordinates. This choice is convenient because it guarantees a good compromise between a fine description and computational time. On the other hand, direct simulations can give specific insights on the mechanisms behind particle–particle interactions, but this microscopic description is achieved at a high-computational cost. The reader is referred to interesting examples of direct simulations.[38,39]

Nevertheless, no matter what approach or length scale is privileged, a model able to capture the well-known shear thinning and normal stress differences in all the concentration regimes of CNT suspensions is still missing in the literature. In this work we favor the mesoscopic scale and propose a novel expression for the lubrication force, which is nonlinear with respect to the relative particle velocity at the contact point. A new rheological model is developed and a new conformation tensor is obtained. In addition, the modified Fokker-Planck equation is numerically solved for steady shear flow, eliminating the inconvenient introduction of closure approximations. The new model contains only four adjustable parameters obtained by fitting experimental data, and its predictions are confronted for two different systems to cover both micro- and nanoscale particles. The first system is composed of CNTs dispersed in an epoxy matrix, and the second consists of a glass fiber-filled polybutene.

Model Formulation

Definitions and hypotheses

A representative volume element (RVE) containing a large number of rods is chosen large enough to have the same behavior as the bulk of the suspension. The number of particles per unit volume is n and the particle volume fraction is represented by ϕ. In the following, the superscript α refers to the test rod while β is used for the neighboring rods. The mass center position of the test rod is defined by the vector $\mathbf{r}_C^{\alpha}$ expressed with respect to a fixed coordinate system $\mathbf{R}$.

The unit vector $\mathbf{p}^{\alpha}$ along the major axis of the rod describes its orientation. The arc length, s^{α}, is measured along the rod axis with $s^{\alpha}=0$ at the center. The rod orientation contained in the RVE can be calculated using the orientation distribution function $\psi_{\mathbf{p}^{\alpha}}$ which is a continuous function of the unit vector $\mathbf{p}^{\alpha}$ over the RVE. Each element of fluid has a velocity in $\mathbf{R}$, and the surrounding fluid angular velocity is defined by $\mathbf{\Omega}^{\infty}=\frac{1}{2}\nabla\times\mathbf{v}^{\infty}$. The model is based on the following hypotheses

1. All particles are considered as straight and rigid rods of uniform length L and constant diameter D.
2. The bulk flow is assumed to be homogeneous, whereas the velocity gradient is constant over the rod length ($\nabla\mathbf{v}^{\infty}=\boldsymbol{\kappa}^{\dagger}$), so the fluid velocity is given by $\mathbf{v}^{\infty}=\boldsymbol{\kappa}\cdot\mathbf{r}_{\mathbf{C}}^{\alpha}$.
3. The suspended rods are assumed to be distributed uniformly, i.e., there is no concentration gradient.
4. The particles are considered inertialess and the gravitational effect is negligible.
5. The matrix is assumed to be incompressible and a continuous Newtonian medium with a viscosity η_0. The fluid motion is determined by the Stokes equation (negligible translational and rotational fluid inertia).
6. The particle–particle interaction force is nonlinear (power-law form) with respect to the relative velocity at the contact point.
7. Affine motion and rotation are assumed.
8. The particles have large aspect ratio, $r=L/D\gg 1$, and, hence, Brownian motion is neglected.

Equations for rod motion

Following Kim and Karrila[40] and Férec et al.,[34] we assume that the test rod α suspended in a Newtonian fluid is subjected to an external force caused by a neighboring interacting rod β. For the case of rod motion with interactions, the time evolution for a test prolate spheroid α, written in $\mathbf{R}$, is

$$\dot{\mathbf{p}}^{\alpha}=\boldsymbol{\varpi}^{\alpha}\times\mathbf{p}^{\alpha}=\left[\mathbf{\Omega}^{\infty}+\mathbf{C}^{-1}\cdot\left(\mathbf{H}:\dot{\boldsymbol{\gamma}}+\mathbf{T}_{\mathbf{I}}\right)\right]\times\mathbf{p}^{\alpha}, \tag{2}$$

where $\boldsymbol{\varpi}^{\alpha}$ is the angular velocity of rod α and $\mathbf{T}_{\mathbf{I}}$ represents the global torque due to the interactions between the test rod α and all neighboring rods. The three terms on the righthand-side of Eq. 2 refer to the rotations due to the rigid-body, the fluid deformation and the interaction torque, respectively. $\mathbf{C}$ and $\mathbf{H}$ are resistance tensors expressed as $\mathbf{C}=\eta_0 L^3[Y_C\boldsymbol{\delta}+(X_C-Y_C)\mathbf{p}^{\alpha}\mathbf{p}^{\alpha}]$ and $\mathbf{H}=-\frac{1}{2}\eta_0 L^3 Y_H(\boldsymbol{\varepsilon}\cdot\mathbf{p}^{\alpha})\mathbf{p}^{\alpha}$, respectively, where $\boldsymbol{\varepsilon}$ is the third-order permutation tensor and X_C, Y_C and Y_H are resistance functions. For the dilute regime (low-concentration suspensions), we find that the rotational drag coefficients are expressed as $X_C=4\pi/r^2$ and $Y_C=1/6$.

To calculate the overall interaction torque $\mathbf{T}_{\mathbf{I}}$, it is necessary to integrate the differential interaction moment $d\mathbf{T}_{\mathbf{I}}$, which is simply the lever arm times the applied differential force $d\mathbf{f}_{\mathbf{I}}$

$$d\mathbf{T}_{\mathbf{I}}=s^{\alpha}\mathbf{p}^{\alpha}\times d\mathbf{f}_{\mathbf{I}}. \tag{3}$$

If a linear lubrication is assumed,[34] the interaction force results in

$$\mathbf{f}_{\mathbf{I}}=D\eta_0 k\Delta\dot{\mathbf{r}}, \tag{4}$$

where k is a dimensionless geometric factor and $\Delta\dot{\mathbf{r}}$ is the time derivative of the shortest distance between two fibers $\Delta\mathbf{r}$. However, while two rods approach each other, the fluid between them is squeezed and this causes a flow that is a nonlinear function of $\Delta\dot{\mathbf{r}}$. To take into account this effect, we propose a new expression for $\mathbf{f}_{\mathbf{I}}$

$$\mathbf{f}_{\mathbf{I}}=Dkb(\Delta\dot{\mathbf{r}}\cdot\Delta\dot{\mathbf{r}})^{\frac{m-1}{2}}\Delta\dot{\mathbf{r}}, \tag{5}$$

where b and m are the consistency and the power-law exponent, respectively, of the rod-rod interaction force. We note that the last equation reduces to Eq. 4 when $m=1$ and $b=\eta_0$.

To satisfy the requirement for material objectivity, the relative rod velocity $\Delta\dot{\mathbf{r}}$, has to be expressed in a co-rotational frame (denoted by the superscript *crf*), and, thus, it reduces to the following form[34]

$$\Delta\dot{\mathbf{r}}^{\mathrm{crf}}=\frac{s^{\beta}}{2}\left(\dot{\boldsymbol{\gamma}}\cdot\mathbf{p}^{\beta}-\dot{\boldsymbol{\gamma}}:\mathbf{p}^{\beta}\mathbf{p}^{\beta}\mathbf{p}^{\beta}\right)-\frac{s^{\alpha}}{2}\left(\dot{\boldsymbol{\gamma}}\cdot\mathbf{p}^{\alpha}-\dot{\boldsymbol{\gamma}}:\mathbf{p}^{\alpha}\mathbf{p}^{\alpha}\mathbf{p}^{\alpha}\right) \tag{6}$$

The expression of $\Delta\dot{\mathbf{r}}^{\mathrm{crf}}$ is then substituted in Eq. 5 to calculate the interaction force. In doing so, we first calculate the dot product in Eq. 7

$$\begin{aligned}\Delta\dot{\mathbf{r}}^{crf}\cdot\Delta\dot{\mathbf{r}}^{crf}=&\left(\frac{s^{\beta}}{2}\right)^2\left[\dot{\boldsymbol{\gamma}}^2:\mathbf{p}^{\beta}\mathbf{p}^{\beta}-\left(\dot{\boldsymbol{\gamma}}:\mathbf{p}^{\beta}\mathbf{p}^{\beta}\right)^2\right]\\&+\left(\frac{s^{\alpha}}{2}\right)^2\left[\dot{\boldsymbol{\gamma}}^2:\mathbf{p}^{\alpha}\mathbf{p}^{\alpha}-\left(\dot{\boldsymbol{\gamma}}:\mathbf{p}^{\alpha}\mathbf{p}^{\alpha}\right)^2\right]\\&-\frac{s^{\alpha}s^{\beta}}{2}\left[\left(\dot{\boldsymbol{\gamma}}\cdot\mathbf{p}^{\beta}-\dot{\boldsymbol{\gamma}}:\mathbf{p}^{\beta}\mathbf{p}^{\beta}\mathbf{p}^{\beta}\right)\cdot\left(\dot{\boldsymbol{\gamma}}\cdot\mathbf{p}^{\alpha}-\dot{\boldsymbol{\gamma}}:\mathbf{p}^{\alpha}\mathbf{p}^{\alpha}\mathbf{p}^{\alpha}\right)\right].\end{aligned} \tag{7}$$

For the sake of simplicity and without losing too much information about the physics (i.e., having the same shear-rate dependency), Eq. 7 can be written as

$$\left(\Delta\dot{\mathbf{r}}^{crf}\cdot\Delta\dot{\mathbf{r}}^{crf}\right)^{\frac{m-1}{2}}\approx\left|\frac{s^{\alpha}}{2}\dot{\boldsymbol{\gamma}}:\mathbf{p}^{\alpha}\mathbf{p}^{\alpha}\right|^{m-1}. \tag{8}$$

This choice is based on two observations. First, the retained scalar has the simplest expression among the other scalars and second, it has a form already reported in the literature by different authors.[41,42] We finally obtain the new form for the interaction force

$$\mathbf{f}_{\mathbf{I}}=Dkb\left|\frac{s^{\alpha}}{2}\dot{\boldsymbol{\gamma}}:\mathbf{p}^{\alpha}\mathbf{p}^{\alpha}\right|^{m-1}\Delta\dot{\mathbf{r}}^{crf}. \tag{9}$$

In order to calculate the elementary interaction force, we need to weight $\mathbf{f}_{\mathbf{I}}$ by the contact probability P_C that represents the probability that a neighboring rod interacts with the test rod. Doi and Edwards[43], and then Sandstrom[29] have proposed an evaluation of this probability as

$$P_C=2nD|\mathbf{p}^{\alpha}\times\mathbf{p}^{\beta}|\psi_{\mathbf{p}^{\beta}}d\mathbf{p}^{\beta}ds^{\alpha}ds^{\beta}, \tag{10}$$

where n is the number density of the rods and $\psi_{\mathbf{p}^{\beta}}$ is the probability to find the interacting rod with an orientation $\mathbf{p}^{\beta}$.

Combining Eqs. 9 and 10, the new elementary interaction force can be written as

$$d\mathbf{f}_{\mathbf{I}}=2nD^2kb\left|\frac{s^{\alpha}}{2}\right|^{m-1}\left|\dot{\boldsymbol{\gamma}}:\mathbf{p}^{\alpha}\mathbf{p}^{\alpha}\right|^{m-1}\Delta\dot{\mathbf{r}}^{crf}\left|\mathbf{p}^{\alpha}\times\mathbf{p}^{\beta}\right|\psi_{\mathbf{p}^{\beta}}d\mathbf{p}^{\beta}ds^{\alpha}ds^{\beta}. \tag{11}$$

Once we obtain the expression for $d\mathbf{f}_{\mathbf{I}}$, it is possible to evaluate the global torque $\mathbf{T}_{\mathbf{I}}$, integrating Eq. 3 over the neighboring and test rod lengths and over all directions of $\mathbf{p}^{\beta}$. This is

equivalent in saying that the "interaction event" can happen with the same probability at any combination of points on the test and neighboring rods (described by the arc lengths s^{α} and s^{β}), but the rod-rod interaction depends on the orientation of the neighboring rods. With these considerations, the global torque is evaluated and consequently, the expression of the orientation time evolution for the test fiber α is obtained

$$\dot{\mathbf{p}}^{\alpha}=\dot{\mathbf{p}}_H^{\alpha}-\phi M_I\int\frac{1}{2}(\dot{\boldsymbol{\gamma}}\cdot\mathbf{p}^{\alpha}-\dot{\boldsymbol{\gamma}}:\mathbf{p}^{\alpha}\mathbf{p}^{\alpha}\mathbf{p}^{\alpha})|\mathbf{p}^{\alpha}\times\mathbf{p}^{\beta}| \\ |\dot{\boldsymbol{\gamma}}:\mathbf{p}^{\alpha}\mathbf{p}^{\alpha}|^{m-1}\psi_{\mathbf{p}^{\beta}}d\mathbf{p}^{\beta}, \tag{12}$$

where ϕ is the volume fraction of the rods and $M_I\equiv\frac{kbL^{m-1}}{2^{2m-3}(m+2)\eta_0\pi Y_C}$, called rod-rod interaction intensity factor, and $\dot{\mathbf{p}}_H^{\alpha}$ is given by the Jeffery equation[18] with $\lambda=1$

$$\dot{\mathbf{p}}_H^{\alpha}=-\frac{1}{2}\boldsymbol{\omega}\cdot\mathbf{p}^{\alpha}+\frac{1}{2}(\dot{\boldsymbol{\gamma}}\cdot\mathbf{p}^{\alpha}-\dot{\boldsymbol{\gamma}}:\mathbf{p}^{\alpha}\mathbf{p}^{\alpha}\mathbf{p}^{\alpha}). \tag{13}$$

Following Folgar and Tucker,[22] we consider that the interactions also modify the fiber rotation, and a perturbation velocity, proportional to the effective deformation rate $|\dot{\gamma}|$, is introduced

$$\dot{\mathbf{p}}^{\alpha}=\dot{\mathbf{p}}_H^{\alpha}-\phi M_I\int\frac{1}{2}\left(\dot{\boldsymbol{\gamma}}\cdot\mathbf{p}^{\alpha}-\dot{\boldsymbol{\gamma}}:\mathbf{p}^{\alpha}\mathbf{p}^{\alpha}\mathbf{p}^{\alpha}+2q|\dot{\gamma}|\frac{\partial\ln\psi_{\mathbf{p}^{\alpha}}}{\partial\mathbf{p}^{\alpha}}\right)|\mathbf{p}^{\alpha}\times\mathbf{p}^{\beta}| \\ |\dot{\boldsymbol{\gamma}}:\mathbf{p}^{\alpha}\mathbf{p}^{\alpha}|^{m-1}\psi_{\mathbf{p}^{\beta}}d\mathbf{p}^{\beta}, \tag{14}$$

where q is a dimensionless interaction coefficient. This diffusional term (the third term in the brackets in Eq. 14 is not due to the Brownian motion, but represents the rotational fluctuations undergoing by the test fiber, when the suspension is under flow.

Rod Orientation Distribution

A suspension is composed of a multitude of particles dispersed in a medium, and to deal with a rod population instead of a single rod, it is necessary to use the orientation distribution function $\psi_{\mathbf{p}^{\alpha}}$.[23] Thus, the probability to find a particle between $\mathbf{p}^{\alpha}$ and $(\mathbf{p}^{\alpha}+d\mathbf{p}^{\alpha})$ is represented by $\psi_{\mathbf{p}^{\alpha}}$. Considering that when a particle leaves one orientation it must appear in another one, $\psi_{\mathbf{p}^{\alpha}}$ can be regarded as a convected scalar. From Bird et al.,[44] the continuity relation can be expressed as

$$\frac{D}{Dt}\psi_{\mathbf{p}^{\alpha}}=-\frac{\partial}{\partial\mathbf{p}^{\alpha}}\cdot\left(\dot{\mathbf{p}}^{\alpha}\psi_{\mathbf{p}^{\alpha}}\right), \tag{15}$$

where D/Dt represents the material derivative. Before combining the last expression with the equation of motion, it is convenient to rewrite Eq. 15 in a more compact way. First we define two new expressions

$$\lambda_{\mathbf{p}^{\alpha}}=1-\phi M_I\int|\mathbf{p}^{\alpha}\times\mathbf{p}^{\beta}||\dot{\boldsymbol{\gamma}}:\mathbf{p}^{\alpha}\mathbf{p}^{\alpha}|^{m-1}\psi_{\mathbf{p}^{\beta}}d\mathbf{p}^{\beta}, \tag{16}$$

$$\dot{\mathbf{p}}_I^{\alpha}=-\frac{1}{2}\boldsymbol{\omega}\cdot\mathbf{p}^{\alpha}+\frac{1}{2}\lambda_{\mathbf{p}^{\alpha}}\left(\dot{\boldsymbol{\gamma}}\cdot\mathbf{p}^{\alpha}-\dot{\boldsymbol{\gamma}}:\mathbf{p}^{\alpha}\mathbf{p}^{\alpha}\mathbf{p}^{\alpha}\right), \tag{17}$$

where $\dot{\mathbf{p}}_I^{\boldsymbol{\alpha}}$ reduces to the Jeffery equation[18] with $\lambda=1$ when the concentration of particles in the system tends toward zero. According to the aforementioned definitions, it is possible now to rewrite Eq. 14 as follows

$$\dot{\mathbf{p}}^{\alpha}=\dot{\mathbf{p}}_I^{\alpha}-2q|\dot{\gamma}|\left(1-\lambda_{\mathbf{p}^{\alpha}}\right)\frac{\partial\ln\psi_{\mathbf{p}^{\alpha}}}{\partial\mathbf{p}^{\alpha}}. \tag{18}$$

Finally, we can obtain the time evolution for the probability distribution function by substituting Eq. 18 in Eq. 15

$$\frac{D}{Dt}\psi_{\mathbf{p}^{\alpha}}=-\frac{\partial}{\partial\mathbf{p}^{\alpha}}\cdot\left(\dot{\mathbf{p}}_I^{\alpha}\psi_{\mathbf{p}^{\alpha}}\right)+2q|\dot{\gamma}|\frac{\partial}{\partial\mathbf{p}^{\alpha}}\cdot\left[\left(1-\lambda_{\mathbf{p}^{\alpha}}\right)\frac{\partial\psi_{\mathbf{p}^{\alpha}}}{\partial\mathbf{p}^{\alpha}}\right]. \tag{19}$$

This expression simplifies into the pure convective Fokker-Planck equation[45] when the concentration of particles is very low.

Stress Determination

Following to Férec et al.,[34] the overall stress is the sum of the matrix, the hydrodynamic and the rod interactions contributions, and, hence, the deviatoric form of the stress $\boldsymbol{\tau}$ becomes

$$\boldsymbol{\tau}=\eta_0\dot{\boldsymbol{\gamma}}+\eta_0\phi N_P\dot{\boldsymbol{\gamma}}:\mathbf{a_4}+n\int\int s^{\alpha}\mathbf{p}^{\alpha}d\mathbf{f_I}\psi_{\mathbf{p}^{\alpha}}d\mathbf{p}^{\alpha}, \tag{20}$$

where $N_P=X_Ar^2/6\pi$, X_A is the parallel drag coefficient of the rods and $\mathbf{a_4}$ is the well-known fourth-order orientation tensor defined by Advani and Tucker[23]

$$\mathbf{a_4}=\int\mathbf{p}^{\alpha}\mathbf{p}^{\alpha}\mathbf{p}^{\alpha}\mathbf{p}^{\alpha}\psi_{\mathbf{p}^{\alpha}}d\mathbf{p}^{\alpha}. \tag{21}$$

Developing the integral in Eq. 20 using Eqs. 6 and 11, the contribution to the stress due to rod interactions is obtained

$$\boldsymbol{\tau}_{\mathbf{I}}=n\int\int s^{\alpha}\mathbf{p}^{\alpha}d\mathbf{f_I}\psi_{\mathbf{p}^{\alpha}}d\mathbf{p}^{\alpha}=2\phi^2M_I\frac{r^2\eta_0Y_C}{\pi}\dot{\boldsymbol{\gamma}}:\mathbf{b_4}^{(m)}, \tag{22}$$

with $\mathbf{b_4}^{(m)}$, the new form of the interaction tensor, defined as

$$\mathbf{b_4}^{(m)}=\int\int\mathbf{p}^{\alpha}\mathbf{p}^{\alpha}\mathbf{p}^{\alpha}\mathbf{p}^{\alpha}|\mathbf{p}^{\alpha}\times\mathbf{p}^{\beta}||\dot{\boldsymbol{\gamma}}:\mathbf{p}^{\alpha}\mathbf{p}^{\alpha}|^{m-1}\psi_{\mathbf{p}^{\alpha}}\psi_{\mathbf{p}^{\beta}}d\mathbf{p}^{\alpha}d\mathbf{p}^{\beta}. \tag{23}$$

The interaction tensor is completely symmetric and it shows a direct dependence on the rate of deformation. Finally, the total stress tensor accounting the effects of rod interactions is given by

$$\boldsymbol{\sigma}=-P\boldsymbol{\delta}+\eta_0\dot{\boldsymbol{\gamma}}+\phi\eta_0X_A\frac{r^2}{6\pi}\dot{\boldsymbol{\gamma}}:\mathbf{a_4}+2\phi^2M_I\frac{r^2\eta_0Y_C}{\pi}\dot{\boldsymbol{\gamma}}:\mathbf{b_4}^{(m)}, \tag{24}$$

where P is the pressure. We note that Eq. 24 reduces to the constitutive equation proposed by Férec et al.[34] for $m=1$ and $b=\eta_0$. Moreover, when the rod volume fraction ϕ, is very small, the contribution due to interactions is negligible and the total stress reduces to that obtained by Dinh and Armstrong,[19] which is valid in the dilute concentration regime.

Numerical Method

For the case of steady-state shear flow, the viscosity and the first normal stress difference are deduced from Eq. 24 and can be written as

$$\eta=\eta_0+2\phi\eta_0N_Pa_{1122}+4\phi^2M_I\frac{r^2\eta_0Y_C}{\pi}b_{1122}{}^{(m)} \\ N_1=2\phi\eta_0N_P\dot{\gamma}_{21}(a_{1112}-a_{1222}) \\ +4\phi^2M_I\frac{r^2\eta_0Y_C}{\pi}\dot{\gamma}_{21}\left(b_{1112}{}^{(m)}-b_{1222}{}^{(m)}\right). \tag{25}$$

Equation 25 show that key components of the fourth-order orientation and interaction tensors are needed to evaluate the viscosity and the first normal stress material functions.

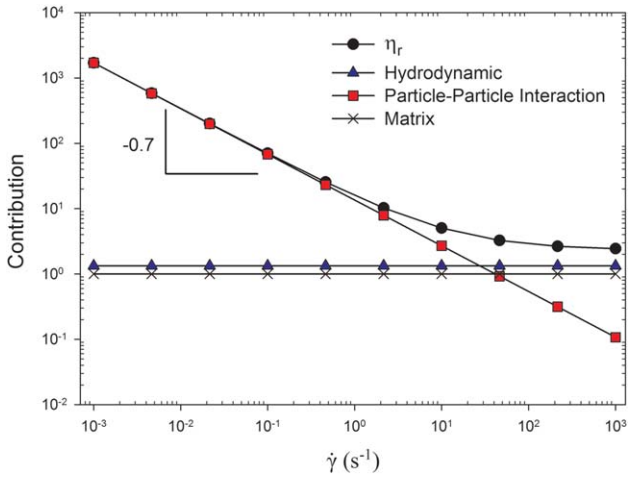

Figure 1. Individual and overall contributions to the steady-state reduced viscosity of a filled system in simple shear flow.

The results were obtained in the case of isotropic orientation distribution and $m = 0.3$. [Color figure can be viewed in the online issue, which is available at wileyonlinelibrary.com.]

Generally closure approximations are used to express the fourth-order tensors in terms of the second-order ones.[46–49] Even though closure approximations are more and more accurate, they always lead to some unavoidable errors. To circumvent this barrier, a possible strategy is to use the probability distribution function evaluated for steady-state. Hence, Eq. 19 becomes

$$\frac{\partial}{\partial \mathbf{p}^{\alpha}} \cdot \left(\dot{\mathbf{p}}_I^{\alpha} \psi_{\mathbf{p}^{\alpha}} \right) = 2q|\dot{\gamma}| \frac{\partial}{\partial \mathbf{p}^{\alpha}} \cdot \left[\left(1 - \lambda_{\mathbf{p}^{\alpha}}\right) \frac{\partial \psi_{\mathbf{p}^{\alpha}}}{\partial \mathbf{p}^{\alpha}} \right]. \qquad (26)$$

This Fokker-Planck equation is strongly nonlinear as both $\dot{\mathbf{p}}_I^{\alpha}$ and $\lambda_{\mathbf{p}^{\alpha}}$ are functions of $\psi_{\mathbf{p}^{\alpha}}$. Therefore, no simple analytic solution exists and a numerical resolution is required. Eq. 26 is numerically solved using a finite volume method as previously performed by Férec et al.[49] (see Férec et al.[49] for more details about the mesh and the treatment of the periodic boundary conditions). The central scheme has been implemented to interpolate properties between the nodes. To obtain a physically steady-state solution, a constraint is added to the numerical system to respect the normalization condition. For a given shear rate, the nonlinear terms are evaluated using successive iterations for the probability distribution function, starting with an initial guess of $1/4\pi$. Convergence is reached when the error between two successive iterations is less than 10^{-3}. Once the distribution function is numerically computed, the orientation and interaction tensor components are straightforwardly obtained for any shear rate using Eqs. 21 and 23.

Isotropic orientation distribution

To understand how the model predictions are influenced by the nonlinear interactions, a first set of simulations was computed imposing an isotropic orientation distribution. This condition was chosen because it guarantees the maximum number of interactions at each shear rate, and, hence, it enhances the effect of the interactions on the overall computations. All the predictions presented in this section and the next were obtained for the following conditions: $\eta_0 = 25$ Pa·s, $\phi = 0.10$ and $r = 30$. In the case of constant isotropic orientation distribution, the only adjustable parameters are M_I, N_P and m. While m is responsible for how the interaction contribution in the macroscopic stress tensor depends on the shear rate, M_I and N_P that control the intensity of the mechanical (rod–rod) and hydrodynamic interactions, respectively, are taken to be both equal to 100, which is a typical value for our experimental suspensions. In the case of simple shear flow and for $m = 0.3$, the different contributions to the steady-state reduced viscosity of a filled system are illustrated in Figure 1. The hydrodynamic contribution is independent of the shear rate while the one due to rod-rod interactions show a decreasing trend. At low-shear rates, the mechanical (rod-rod) interactions are the dominant mechanism while, at high-shear rates, the hydrodynamic contribution becomes controlling. The transition between the two mechanisms is clearly represented by the trend of the reduced viscosity that goes from a shear-thinning behavior to a plateau-like at high-shear rates that approaches the viscosity of the matrix. In the case of an isotropic orientation distribution the first normal stress difference is null, independently of the shear rate, because the components of $\mathbf{a_4}$ and $\mathbf{b_4}^{(m)}$ involved in the expression of N_1 are equal to each other.

The model was also tested for the case of elongational flow, resulting in similar behaviors (results not shown here).

Parametric analysis

When the condition on the isotropic orientation distribution is removed, the model has a fourth adjustable parameter q, which controls the perturbation on the particle rotational velocity due to the interactions, and that is modeled mathematically as a diffusion term in Eq. 19. The effects of q and N_P on the model predictions are well-known from the literature.[34,50] The steady-state viscosity is almost independent of q whereas it increases with N_P, and the first normal stress difference rises with q and N_P. With the introduction of the nonlinear elementary rod-rod interaction force, two additional adjustable parameters have entered the model (M_I and m) and the interactions between particles can also be controlled by tuning their values. The set of parameters used for the following simulation results are reported in Table 1.

Increasing M_I (Test A) is equivalent to increasing the intensity of the interactions and this is clearly shown by the higher steady shear viscosity and enhanced shear thinning illustrated in Figure 2. By the analysis of the second-order tensor component a_{11} (where 1 is the flow direction), the interactions prevent rods from getting aligned in the flow direction, which is physically realistic as depicted in Figure 3. Modern theories of anisotropic particle suspensions attribute the origin of the normal force to particles sticking out of the flow plane due to interactions.[19,22,34] The model predictions are in agreement with this last statement as shown by

Table 1. Parameters used for the Parametric Analysis on the Steady Shear Viscosity, First Normal Stress Difference and $\mathbf{a_2}$ Component Predictions

	Test A	Test B
N_P	100	100
M_I (s^{m-1})	[0.1, 0.3, 0.5, 0.7]	0.5
q	0.1	0.1
m	0.5	[0.3, 0.5, 0.7, 1]

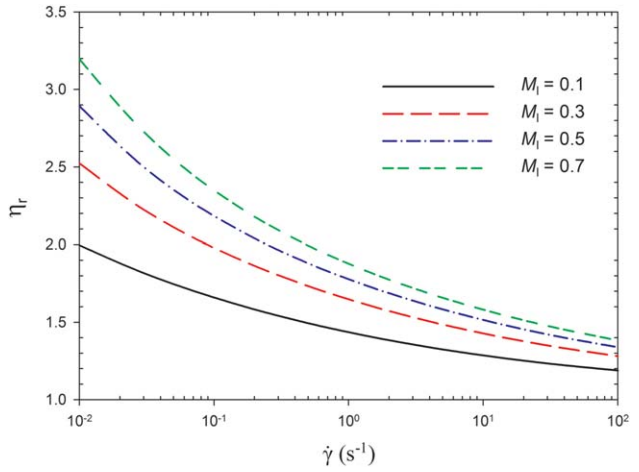

Figure 2. Reduced steady-shear viscosity predictions as function of shear rate for different values of M_l.

The values of the other three adjustable parameters are reported in Table 1 (Test A). [Color figure can be viewed in the online issue, which is available at wileyonlinelibrary.com.]

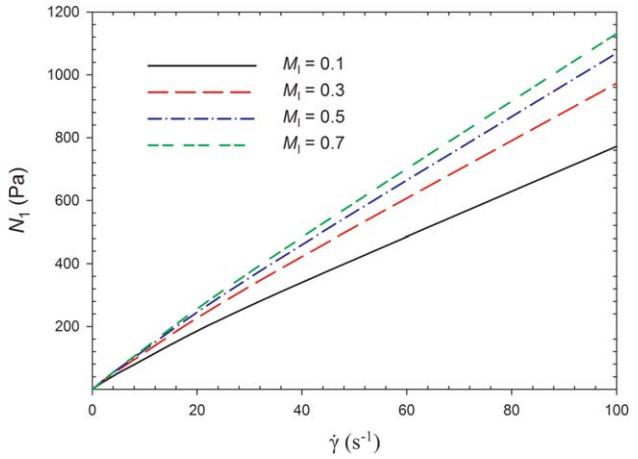

Figure 4. First normal stress difference predictions as function of shear rate for various values of M_l.

The values of the three other adjustable parameters are reported in Table 1 (Test A). [Color figure can be viewed in the online issue, which is available at wileyonlinelibrary.com.]

the increase of the first normal stress difference presented in Figure 4. Conversely, the initial condition of an isotropic orientation is characterized by the obvious fact that the particle orientation distribution is spherically symmetric at equilibrium. However, shear flow will distort the distribution, making it "ellipsoidal". Normal stresses can be associated with the tendency of the distorted distribution to relax back to the spherical shape, implying a compression orthogonal to the shear direction. The rod–rod interactions influence how the orientation distribution is distorted by the shear flow.

The effect of parameter m on the reduced steady shear viscosity is highlighted in Figure 5 (parameters of Test B in Table 1). Varying m from 0 to 1, a full spectrum of behavior is obtained, from shear thinning ($m < 1$) to Newtonian ($m = 1$); hence, parameter m clearly controls the dependency with shear rate of the interactions.

The first normal stress difference does not show significant variations as illustrated in Figure 6; however, it shows a decreasing trend with increasing value of m. This effect is more significant at high-shear rates since m influences the dependency of the interactions with shear rate. Lower values of N_1 imply a more oriented network of rods and this scenario is confirmed by the behavior of a_{11} in Figure 7.

In addition, the model is able to predict a shear-thickening behavior for ($m > 1$) (results not shown).

Materials and Experimental Methodology

A Newtonian low-viscosity matrix was chosen to emphasize the rheological features due to the carbon nanotubes in the suspension. An epoxy (Epon 828, HEXION Specialty Chemicals, Inc.) with a density of 1.16 g/mL and a viscosity

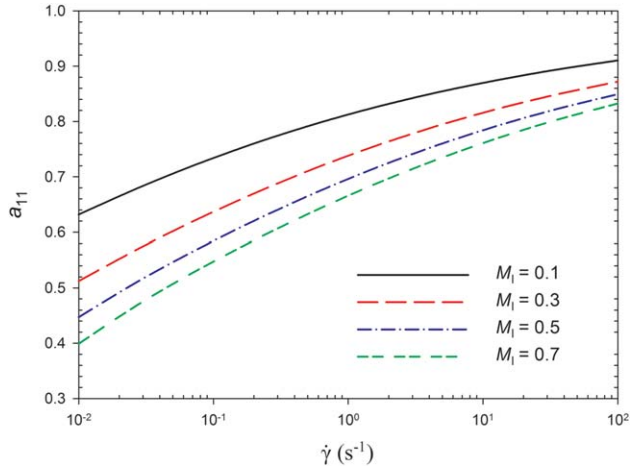

Figure 3. Component a_{11} of the second-order orientation tensor as function of shear rate for different values of M_l.

The values of the other three adjustable parameters are reported in Table 1 (Test A). [Color figure can be viewed in the online issue, which is available at wileyonlinelibrary.com.]

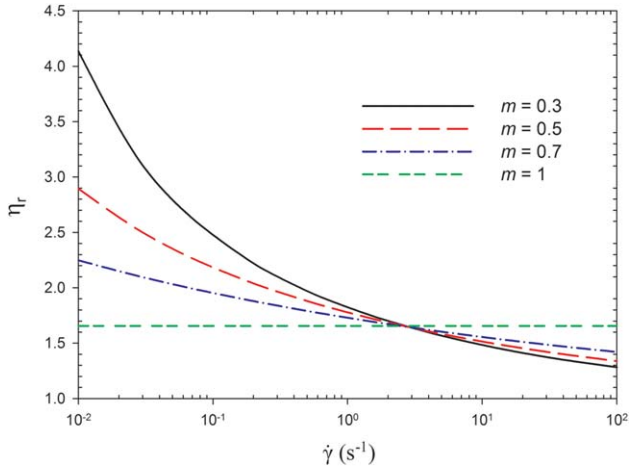

Figure 5. Reduced steady shear viscosity predictions as function of shear rate for different values of m.

The values of the other three adjustable parameters are reported in Table 1 (Test B). [Color figure can be viewed in the online issue, which is available at wileyonlinelibrary.com.]

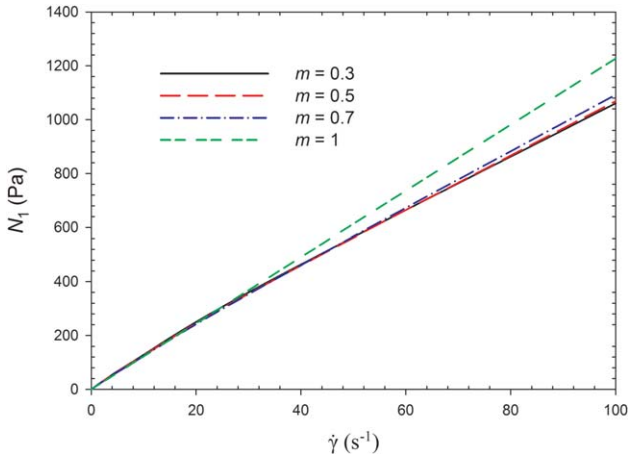

Figure 6. First normal stress difference predictions as function of shear rate for different values of *m*.

The values of the other three adjustable parameters are reported in Table 1 (Test B). [Color figure can be viewed in the online issue, which is available at wileyonlinelibrary.com.]

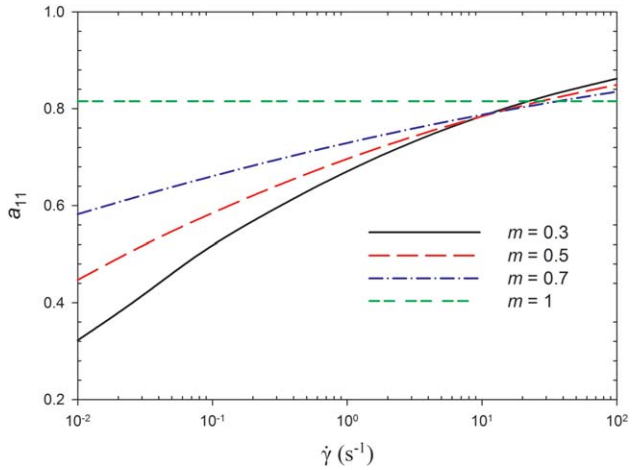

Figure 7. Component a_{11} of the second-order orientation tensor as function of shear rate for different values of *m*.

The values of the other three adjustable parameters are reported in Table 1 (Test B). [Color figure can be viewed in the online issue, which is available at wileyonlinelibrary.com.]

of 12.3 Pa.s (at 25 °C) was used as the dispersing medium. Multiwalled carbon nanotubes (MWCNTs) from Cheap Tubes, Inc., were characterized in a previous work.[12] The main characteristics of the suspensions investigated in this work are given in Table 2. The table also reports the corresponding characteristics of glass fiber suspensions in a polybutene taken from Sepehr et al.[1] In addition, the CNTs can be considered as rigid rods in the range of shear rates studied here according to Switzer and Klingenberg[38] assuming a Young modulus of 40 GPa.[5]

The suspensions of CNT-epoxy were prepared using an EXAKT three-roll mill (from EXAKT Technologies, Inc.) at room temperature. The CNTs were mixed as received with the epoxy without any surfactant or additive. The samples were initially manually blended with a spatula in a glovebox, and then were poured into the three-roll mill (3RM). To break the CNT agglomerates and avoid a reduction in the aspect ratio during mixing, the gaps between the mill rolls were equally set and gradually reduced from 100 to 5 μm. Each sample was circulated between the gaps of the rolls once at the 100 and 50 μm gap sizes, twice at the 20 and 10 μm gap sizes and four times at the 5 μm gap size. During this procedure, the speed of the rollers was maintained constant at 150 rpm.

In order to verify the degree of dispersion, a suspension containing 4.4 wt % CNTs was prepared and transmission electron microscopy (TEM) analysis was performed after thermal curing. The curing agent used was a commercial product, JEFFAMINE® T-403 polyetheramine. After preparation with the three-roll mill, suspension samples were gently hand-mixed with the curing agent at room temperature to avoid formation of bubbles. The composition of the final system was 32 wt % T-403 and 68 wt % epoxy/CNT suspension. Hence, the addition of T-403 resulted in a dilution of CNTs in the system, from 4.4 to 3 wt %. After mixing with the curing agent, the samples were left to rest for 1 h in a vacuum oven at room temperature to remove any bubbles and finally, always *in vacuo*, the temperature was increased to 80°C for 2 h to obtain a fully set system. TEM analysis was performed on thin sections of samples ultramicrotomed with a diamond knife at room temperature. Figure 8 shows TEM images for two magnifications of the cured sample. Both images depict a good degree of dispersion of the CNTs with the chosen mixing procedure. Only few agglomerates are observable in the lower magnification image (shown by the arrow in Figure 8a) and individual nanotubes, many in contact with neighbors, are detected in the high-magnification view (Figure 8b). We believe that the few small agglomerates, as seen in Figure 8a, have little influence on the rheological behavior of these CNT suspensions.

A Physica MCR502 (Anton Paar) rheometer with a cone-and-plate flow geometry (CP50 with the diameter of 50 mm and an angle of 2°) was used to perform the rheological measurements at 25°C. The cone-and-plate geometry allows a homogeneous shear flow, which makes it preferable not only to achieve precise rheological data but also to recreate the flow conditions used for the model calculations. The gap at the center of the cone is 51 μm, which is about 80 times larger than the average length of the carbon nanotubes. Moreover, the absence of wall effects was assessed by comparing results from the cone-and-plate geometry with data from a parallel-plate flow geometry (PP50 with a diameter of 49.96 mm, 1 mm gap) corrected according to Carreau et al.[51] (data not reported). The temperature during the tests was controlled at 25°C by a Peltier (P-PTD 200) system. All

Table 2. Characteristics of the Materials

Suspensions	Matrix	Viscosity η_0 (Pa.s)	Fiber volume % range	Fiber length L (μm)	Fiber diameter D (μm)	Aspect ratio r
EPO-CNT	Epoxy	12.3	0.59 – 2.36	0.1 – 2.2	$7{\cdot}10^{-3}$ – $2.5{\cdot}10^{-2}$	4 – 314
PB-GF[1]	Polybutene	24.0	1.58 – 7.06	260	14	20

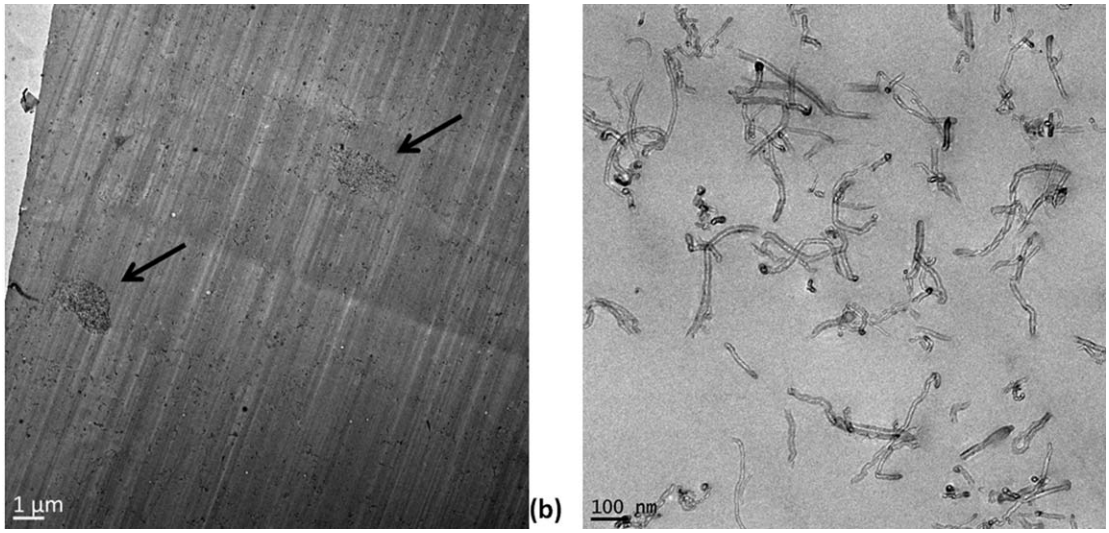

Figure 8. TEM images of a cured suspension containing 3 wt% CNTs at lower (a) and at higher (b) magnification.

The arrows are used to indicate the agglomerates.

experiments were run 1 day after sample preparation to avoid aging effects.

To cover all concentration regimes, four volume fractions of carbon nanotubes were chosen. According to the work of Khalkhal et al.[12], the limits between the different regimes can be distinguished from rheological measurements based on the reduced viscosity η_r as a function of volume fraction ϕ. The authors found that the boundary between the dilute and the semidilute regime was at $\phi \approx 0.9\%$, while the concentrated regime was reached for $\phi \geq 2.05\%$. Hence, one concentration representative of the dilute regime (ϕ=0.59%) or 1 wt %, two for the semidilute (ϕ=1.18%, 1.77%) or 2 and 3 wt %, and one for the concentrated regime were investigated (ϕ=2.36%) or 4 wt %.

Data and Predictions

Network formation, particles orientation and interactions play an important role on the rheological properties of CNT suspensions. While the steady-state viscosity for the neat epoxy is Newtonian over the entire range of shear rate investigated (constant viscosity of 12.3 Pa.s), with the addition of the filler the system exhibits a shear-thinning behavior with a significant enhancement of the viscosity at low-shear rates, as illustrated in Figure 9. The lines are the model predictions using the parameters reported in Table 3 and the aspect ratio for the CNTs of 182, which is consistent with the experimental range reported in Table 2. As stated before, the model contains four independent adjustable parameters: q, N_P, M_I and m. A least-square method was used to solve the fitting problem and only one set of parameters was necessary to predict both the reduced steady-shear viscosity and first normal stress difference (Figure 10) for the four CNT concentrations. The model predicts very well the effect of CNT concentration as well as the shear-thinning behavior.

By increasing the CNT content, nanotube-nanotube interactions become progressively dominant. The higher is the concentration, the smaller the relative interparticle distance. This eventually leads to a percolated network throughout the system which restrains the long-range motion of the polymer chains,[5] responsible for a further increase in the viscosity at low-shear rates. However, the shear flow is able to break down the network between MWNTs and the individual particles get oriented in the flow direction.[4] This promotes the shear-thinning behavior reported in Figure 9. The steady shear viscosity data obeys a power-law expression at low-shear rates. The slope of the log–log plots decreases slightly with the loading, varying from −0.67 (1 wt %) to −0.82 (4 wt %), whereas the model predicts an unique slope of −0.72. Thus, the behavior tends to the solid-like limit, which is characterized by a theoretical slope of −1.

The presence of carbon nanotubes in a Newtonian matrix causes the appearance of normal stresses during shear flow, as shown in Figure 10. Normal stresses increase with shear rate and CNT concentration (data also become less noisy). This suggests that the enhancement of the normal force is a result of the combination of particle interactions[50] and network elasticity developed by the interconnections between

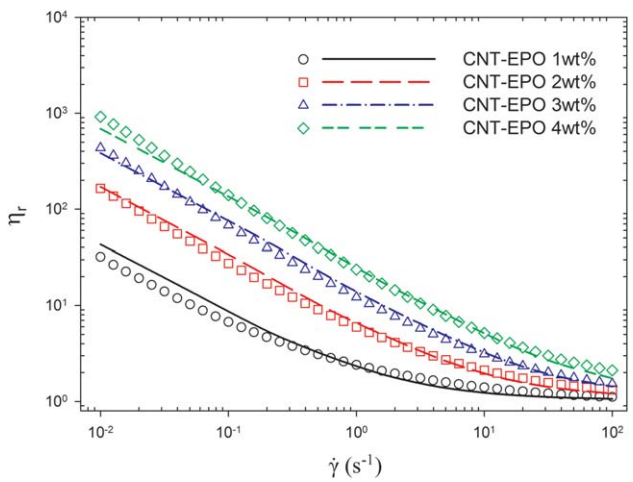

Figure 9. Reduced steady-shear viscosity data (symbols) for the four CNT concentrations dispersed in an epoxy matrix.

The experimental results are compared with the model predictions (lines). The fitting parameter values are reported in Table 3. [Color figure can be viewed in the online issue, which is available at wileyonlinelibrary.com.]

Table 3. Adjustable Parameter Values Obtained by Fitting the Experimental Steady Shear Viscosity and Normal Stress Difference Data for Carbon Nanotubes Dispersed in Epoxy (CNT-EPO) and Glass Fibers Dispersed in Polybutene (PB-GF)[1]

Suspensions	Hydrodynamic coefficient N_P	Interaction coefficient q	Rod-rod Interaction intensity factor M_I (s^{m-1})	Interaction power-law exponent m
EPO-CNT	146.6	0.06	75.1	0.28
PB-GF	82	5.92	0.07	0.77

the high aspect ratio CNTs in the medium. The lines in Figure 10 are the model predictions using the same parameters as for the fitting of the steady shear viscosity of Figure 9 (see Table 3). The model predicts correctly the trend with shear rate; however the effect of CNT concentration is underpredicted. The rod-rod interactions are not sufficient to predict the high values of the first normal stress difference as observed at low shear rates for the more concentrated CNT suspension. This aspect is intrinsically connected with the formation of a network (percolation) resulting from the contact of multiple particles and, hence, another mechanism has to be introduced to describe the network elasticity.

Many authors have reported the establishment of a particle network in their system by showing the classical plateau of the storage modulus (G') at low frequencies in small amplitude oscillatory shear (SAOS) measurements.[2,4,5] In addition, many others have reported the tangent of the phase angle for CNT suspensions showing the transition from a viscous to an elastic system coinciding with the establishment of a network (or percolation threshold).[9,10]

In order to separate the effect of a network formation from those of the particle–particle interactions, it is useful to compare the experimental findings of suspensions of nanoparticles with those of classical microscale suspensions. This helps to highlight the importance of a network on the rheological results of the CNT suspensions, and also to validate the versatility of the model proposed. Hence, the CNT-epoxy system is compared with a Newtonian polybutene filled with glass fibers (data from Sepehr et al.[1]). The information regarding the matrix and the filler are reported and compared with the respective characteristics of the CNT-epoxy system in Table 2.

Three different weight fractions of glass fibers (GFs) were used (4.3% (PB05), 8.7% (PB10), and 17.6% (PB20)). More information regarding the preparation conditions of the suspensions can be found in Sepehr et al.[1] Glass fibers (GFs) do not form networks and, when dispersed in a Newtonian matrix, they do not induce elasticity to the system. Consequently, they show a moderate shear-thinning behavior and no tendency toward an infinite viscosity at low-shear rates (or presence of a yield stress), even at high concentrations. The behavior is illustrated in Figure 11, which compares the steady-shear viscosity data to the model predictions. Since no network is established, the shear thinning must be mainly due to fiber orientation under flow. As for the CNT systems, only one set of the adjustable parameters was required to predict all the experimental findings (Figures 11 and 12). The values of the parameters for the GF systems are also reported in Table 3 and the aspect ratio used in the model is reported in Table 2. The model describes reasonably well the data and the shear thinning is well predicted, but the effect of fiber concentration on the steady-state viscosity is overpredicted. We note from Table 3 that the mechanical (rod-rod) interaction intensity factor (M_I) for the glass fiber suspensions is almost zero (0.07 s^{m-1}) compared to a very large value for the CNT suspensions (75.1 s^{m-1}).

Figure 12 compares the normal stress difference (N_1-N_2) data (obtained from parallel plate geometry) and the model predictions as functions of the shear rate for the different

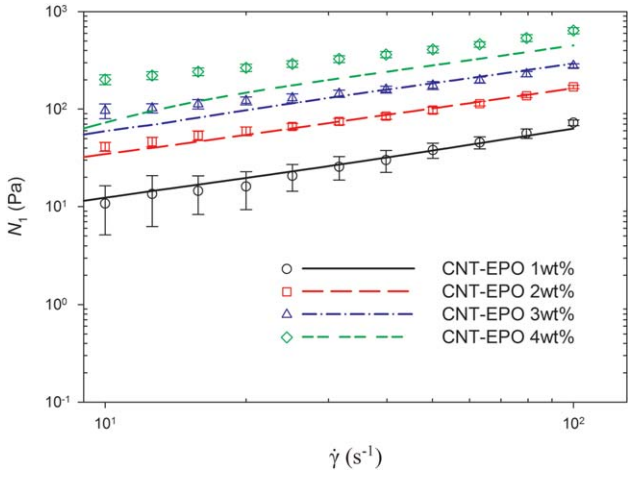

Figure 10. First normal stress difference data (symbols) for the four CNT concentrations dispersed in an epoxy matrix.

The experimental results are compared with the model predictions (lines). The fitting parameter values are reported in Table 3. [Color figure can be viewed in the online issue, which is available at wileyonlinelibrary.com.]

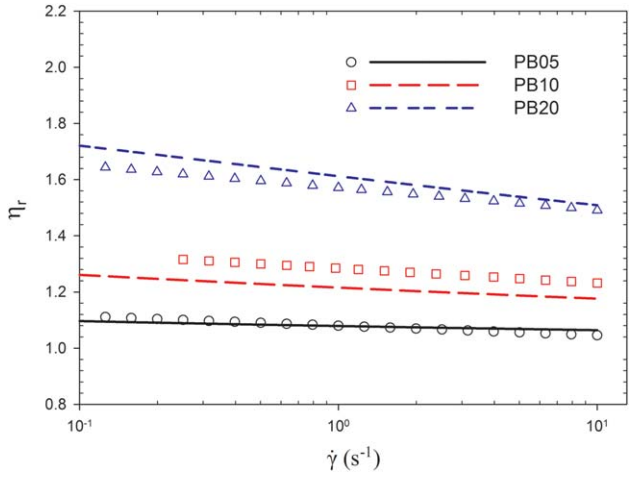

Figure 11. Reduced steady-shear viscosity data (symbols) of the three GF concentrations dispersed in a polybutene matrix.

The experimental results are compared with the model predictions (lines). The fitting parameter values are reported in Table 3. The experimental data are taken from Sepehr et al.[1] [Color figure can be viewed in the online issue, which is available at wileyonlinelibrary.com.]

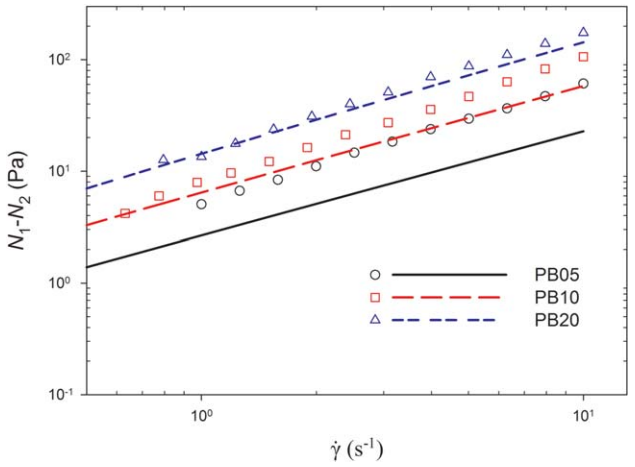

Figure 12. Normal stress difference data (symbols) of the three GF concentrations dispersed in a polybutene matrix.

The experimental results are compared with the model predictions (lines). The fitting parameter values are reported in Table 3. The experimental data are taken from Sepehr et al.[1] [Color figure can be viewed in the online issue, which is available at wileyonlinelibrary.com.]

concentrations of glass fibers dispersed in the polybutene matrix. The same parameters for predicting the viscosity were used (see Table 3). The normal stress difference exhibits a slope of 1 and its magnitude increases with fiber content as fairly well predicted by the model. The effect of concentration is too pronounced as observed by the lower values predicted at the lowest fiber concentration (5 wt %). This behavior has been documented in the literature.[21,52] The enhancement of the normal stresses in the presence of fibers in a Newtonian fluid is largely due to fiber–fiber interactions. The slope of 1 is well predicted by different models[22,33,34] and they all have in common the assumption that collisions between particles are the major cause for nonzero normal stresses in steady-shear flows.

In comparison, the slope of the normal stress difference N_1 between 40 and 100 s^{-1} for the CNT suspensions decreases with CNT content, from 0.93 for the 1 wt % to 0.6 for the 4 wt % (Figure 10). For the suspension with 1 wt % of CNTs, the network is not fully established since the percolation threshold is somewhere between 1 and 2 wt % as shown by Khalkhal et al.[12] This implies that the increase in normal stresses is mainly due to the interactions between the rods. Thus, the N_1 dependency with shear rate for the lowest CNT concentration is similar to the one reported for GFs, and the slope is indeed close to 1 (0.93). However, with increasing concentration of CNTs, or equivalently building a network between the dispersed particles, the system behaves more like a viscoelastic fluid and the first normal stress difference is the result of two contributions: rod-rod interactions and network elasticity. The rod–rod interaction contribution is a linear function of the shear rate, whereas, as shown by the steady-state viscosity in Figure 9, the network tends to be destroyed with the intensity of the shear flow, thus, the network elasticity contribution must decrease with shear rate. Increasing CNT loading, the contribution due to network elasticity is more important, as shown by the high values of N_1 at low-shear rates. Consequently, the relative importance of the network elasticity with respect to the rod-rod interactions grows and, hence, the value of the slope of N_1 vs. $\dot{\gamma}$ (log–log plot) decreases with CNT concentration.

From the model predictions, it is possible to obtain microstructural information. More precisely, the second-order orientation tensor can be used as a compact representation of the overall orientation of the particles without significant loss of information. For carbon nanotube suspensions, the components of the second-order orientation tensor, calculated for the parameter values given in Table 3, are illustrated in Figures 13a and b. Initially, the rods tend toward an isotropic orientation at a shear rate around 10^{-1} s^{-1} for the suspension containing 1 wt % CNT and only at larger shear rates do they orient along the flow direction. Increasing the concentration has an effect also on the position of the a_{11} minimum that is shifted to higher shear rates. Until the shear rate at which the minimum appears, the tendency of the rods to get oriented in the flow direction is overcome by the particle–particle interactions. At higher shear rates the hydrodynamic interactions gain more importance and the rods get oriented. Again, larger is the number of particles dispersed in the system, higher is the average number of contacts for tubes and, hence, the overall degree of orientation is lower.

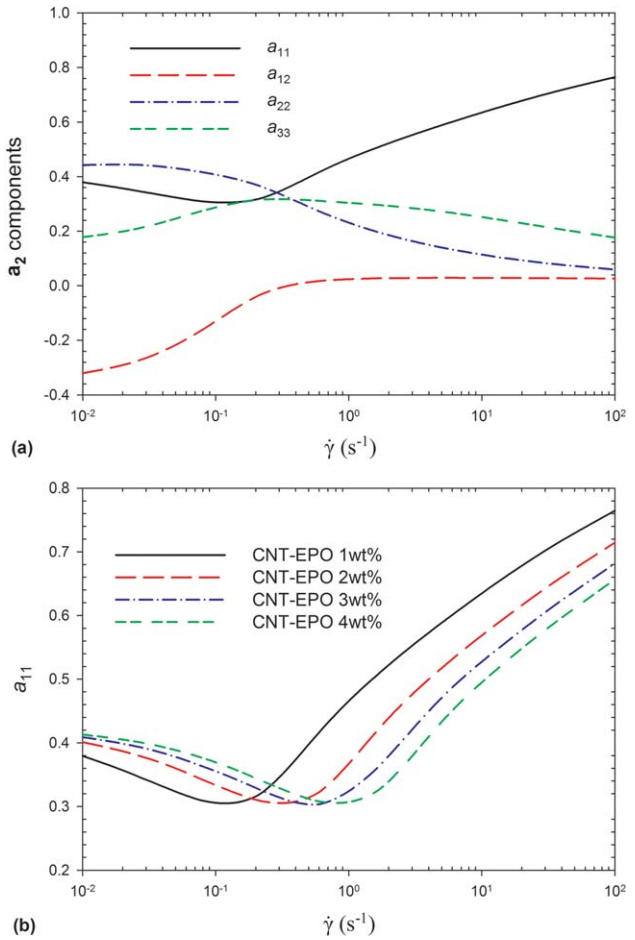

Figure 13. (a) Variations of the a_2 components as functions of shear rate for the 1 wt % CNT suspension, and (b) variation of the a11 component as function of shear rate for various CNT concentrations.

[Color figure can be viewed in the online issue, which is available at wileyonlinelibrary.com.]

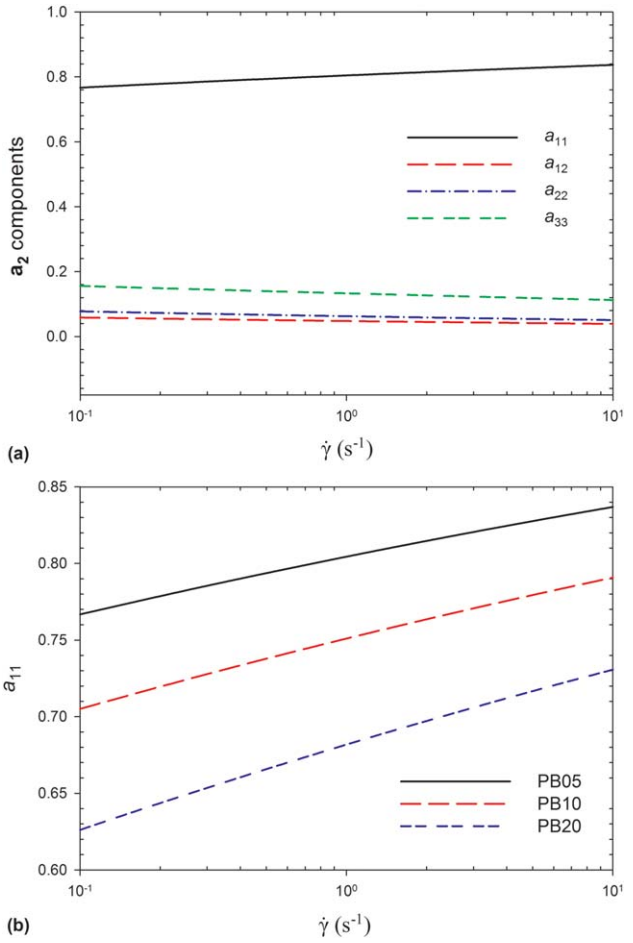

Figure 14. (a) Variations of the a_2 components as functions of shear rate for the 5 wt % GF suspension (PB05), and (b) variation of the a_{11} component as function of shear rate for different GF concentrations.

[Color figure can be viewed in the online issue, which is available at wileyonlinelibrary.com.]

In the case of glass fibers, the components of $\mathbf{a_2}$ show a monotonic behavior as functions of shear rate and the fibers tend to get oriented in the flow direction (Figures 14a and b). With increasing fiber concentration, the fiber–fiber interaction contribution becomes more important, provoking a randomizing effect on the overall orientation distribution and causing a lower degree of orientation, as shown in Figure 14b.

By comparing the two set of parameters reported in Table 3, we underline how the model recognizes the differences between a microsize and a nanosize filled system. In particular, the nature of the interactions for the two systems is completely different and it is characterized by the two parameters M_I and m. In the case of CNTs, the rod-rod interaction intensity factor (M_I) is three orders of magnitude larger than the one for glass fiber suspension, while the interaction power-law exponent (m) shows a stronger dependency on shear rate. The description of the interaction nature obtained from the model is in agreement with the CNTs higher aspect ratio with respect to GFs, and with the additional contribution due to attractive forces for nanoparticles.[39] In addition, we find that the value of N_P for the glass fiber system is very close to that obtained by Sepehr et al.[50] using the Folgar and Tucker[22] model.

Concluding Remarks

Unlike well-known rheological models for anisotropic particle suspensions at the mesoscopic scale, the new constitutive equation proposed in this work includes a term representative of particle–particle interactions that depends directly on the shear rate. Once the solution of the modified Fokker-Planck equation is obtained for steady-state, it provides the orientation distribution function, the viscosity and normal stress differences without the need of closure approximations. As a result of the nonlinear function proposed to describe particle–particle interactions, the relative importance of interaction and hydrodynamic contributions depends on shear rate. For an index m between 0 and 1, particle interactions become predominant at low-shear rates, exhibiting an apparent yield stress as observed for many nondilute suspensions, while at high shear rates the hydrodynamic contribution becomes dominant.

The model predictions are in good agreement with the experimental findings for both the CNT-epoxy and GF-polybutene systems. For the CNT suspensions, the proposed interaction force is not sufficient to completely predict the first normal stress difference data as observed at low-shear rates for the more concentrated suspension. Therefore, another mechanism should be taken into account to fully describe the CNT network elasticity.

Furthermore, the model is found to recognize the differences between micro and nanosize filled composites, mainly distinguishing the relative importance of the particle–particle interactions and network formation.

In this work, we were able to avoid the use of closure approximations by solving numerically the modified Fokker-Planck equation for steady-state. However, closure approximations might be necessary to calculate the predictions in transient flows since the nonlinearity present in the modified Fokker-Planck equation will result in very long computational times. Hence, a closed form for the time evolution of the second-order orientation tensor will need to be developed. Recently, numerical strategies called proper generalized decomposition (PGD)[53,54] have been proposed to overcome the high-dimensional problems (time, physical space and conformational coordinates) involved in complex flows. These techniques may represent alternatives to overcome the limitations of classical approaches.

Acknowledgments

This work was funded by NSERC (Natural Science and Engineering Research Council of Canada). The authors are thankful to Dr. Daniel Therriault for providing access to the three-roll mill at the composite laboratory in the Mechanical Engineering Department of Ecole Polytechnique.

Literature Cited

1. Sepehr M, Carreau PJ, Moan M, Ausias G. Rheological properties of short fiber model suspensions. *J Rheology*. 2004;48(5):1023–1048.
2. Du F, Scogna RC, Zhou W, Brand S, Fischer JE, Winey KI. Nanotube networks in polymer nanocomposites: rheology and electrical conductivity. *Macromolecules*. 2004;37(24):9048–9055.
3. Huang YY, Ahir SV, Terentjev EM. Dispersion rheology of carbon nanotubes in a polymer matrix. *Phys Rev B*. 2006;73(12):125422.

4. Fan Z, Advani SG. Rheology of multiwall carbon nanotube suspensions. *J Rheology*. 2007;51(4):585–604.
5. Hobbie EK, Fry DJ. Rheology of concentrated carbon nanotube suspensions. *The J Chem Phys*. 2007;126(12):124907–124907.
6. Wu D, Wu L, Zhang M. Rheology of multi-walled carbon nanotube/poly(butylene terephthalate) composites. *J Polym Sci Part B: Polym Phys*. 2007;45(16):2239–2251.
7. Song YS, Youn JR. Influence of dispersion states of carbon nanotubes on physical properties of epoxy nanocomposites. *Carbon*. 2005;43(7):1378–1385.
8. Hu G, Zhao C, Zhang S, Yang M, Wang Z. Low percolation thresholds of electrical conductivity and rheology in poly(ethylene terephthalate) through the networks of multi-walled carbon nanotubes. *Polymer*. 2006;47(1):480–488.
9. Abdel-Goad M, Pötschke P. Rheological characterization of melt processed polycarbonate-multiwalled carbon nanotube composites. *J Non-Newtonian Fluid Mech*. 2005;128(1):2–6.
10. Abbasi S, Carreau P, Derdouri A, Moan M. Rheological properties and percolation in suspensions of multiwalled carbon nanotubes in polycarbonate. *Rheologica Acta*. 2009;48(9):943–959.
11. Khalkhal F, Carreau PJ. Critical shear rates and structure build-up at rest in MWCNT suspensions. *J Non-Newtonian Fluid Mech*. 2012; 171-172(0):56–66.
12. Khalkhal F, Carreau PJ, Ausias G. Effect of flow history on linear viscoelastic properties and the evolution of the structure of multiwalled carbon nanotube suspensions in an epoxy. *J Rheology*. 2011; 55(1):153–175.
13. Hobbie EK, Wang H, Kim H, Lin-Gibson S, Grulke EA. Orientation of carbon nanotubes in a sheared polymer melt. *Phys Fluids*. 2003; 15(5):1196–1202.
14. Fan Z, Advani SG. Characterization of orientation state of carbon nanotubes in shear flow. *Polymer*. 2005;46(14):5232–5240.
15. Fry D, Langhorst B, Wang H, et al. Rheo-optical studies of carbon nanotube suspensions. *J Chem Phys*. 2006;124(5):054703.
16. Ma A, Mackley M, Rahatekar S. Experimental observation on the flow-induced assembly of carbon nanotube suspensions to form helical bands. *Rheologica Acta*. 2007;46(7):979–987.
17. Rahatekar SS, Koziol KKK, Butler SA, et al. Optical microstructure and viscosity enhancement for an epoxy resin matrix containing multiwall carbon nanotubes. *J Rheology*. 2006;50(5):599–610.
18. Jeffery GB. The motion of ellipsoidal particles immersed in a viscous fluid. *Proc R Soc London Ser A*. 1922;102:161–179.
19. Dinh SM, Armstrong RC. A rheological equation of state for semiconcentrated fiber suspensions. *J Rheology*. 1984;28(3):207–227.
20. Shaqfeh ESG, Fredrickson GH. The hydrodynamic stress in a suspension of rods. *Phys Fluids a-Fluid Dynam*. 1990;2(1):7–24.
21. Petrich MP, Koch DL, Cohen C. An experimental determination of the stress-microstructure relationship in semi-concentrated fiber suspensions. *J Non-Newtonian Fluid Mech*. 2000;95(2–3):101–133.
22. Folgar FP, Tucker CL. Orientation behavior of fibers in concentrated suspensions. *J Reinf Plast Compos*. 1984;3:99.
23. Advani SG, Tucker CL. The use of tensors to describe and predict fiber orientation in short fiber composites. *J Rheology. Nov* 1987; 31(8):751–784.
24. Bay RS. Fiber Orientation in Injection-Molded Composites: A Comparison of Theory and Experiment [Ph.D. dissertation]. Illinois: University of Illinois at Urbana-Champaign; 1991.
25. Phan-Thien N, Fan XJ, Tanner RI, Zheng R. Folgar-Tucker constant for a fibre suspension in a Newtonian fluid. *J Non-Newtonian Fluid Mech*. 2002;103(2–3):251–260.
26. Ranganathan S, Advani SG. Fiber-fiber interactions in homogeneous flows of nondilute suspensions. *J Rheology*. 1991;35(8):1499–1522.
27. Ma WKA, Chinesta F, Ammar A, Mackley MR. Rheological modeling of carbon nanotube aggregate suspensions. *J Rheology*. 2008; 52(6):1311–1330.
28. Chinesta F. From single-scale to two-scales kinetic theory descriptions of rods suspensions. *Arch Computat Methods Eng*. 2013;20(1):1–29.
29. Sandstrom CR. Interactions and Orientation in Concentrated Suspensions of Rigid Rods: Theory and Experiment [Ph.D. thesis]. Urbana-Champaign, University of Illinois; 1993.
30. Sandstrom CR, Tucker CL. A theory for concentrated fiber suspensions with strong fiber-fiber interactions. *Makromole Chem Macromole Symp*. 1993;68:291–300.
31. Servais C, Luciani A, Manson J-AE. Fiber-fiber interaction in concentrated suspensions: Dispersed fiber bundles. *J Rheology*. 1999; 43(4):1005–1018.
32. Servais C, Manson J-AE, Toll S. Fiber-fiber interaction in concentrated suspensions: Disperse fibers. *J Rheology*. 1999;43(4):991–1004.
33. Djalili-Moghaddam M, Toll S. A model for short-range interactions in fibre suspensions. *J Non-Newtonian Fluid Mech*. 2005;132(1–3): 73–83.
34. Férec J, Ausias G, Heuzey MC, Carreau PJ. Modeling fiber interactions in semiconcentrated fiber suspensions. *J Rheology*. 2009;53(1): 49–72.
35. Le Corre S, Caillerie D, Orgéas L, Favier D. Behavior of a net of fibers linked by viscous interactions: theory and mechanical properties. *J Mech Phys Solids*. 2004;52(2):395–421.
36. Le Corre S, Dumont P, Orgeas L, Favier D. Rheology of highly concentrated planar fiber suspensions. *J Rheology*. 2005;49(5):1029–1058.
37. Guiraud O, Orgeas L, Dumont PJJ, Roscoat SRD. Microstructure and deformation micromechanisms of concentrated fiber bundle suspensions: An analysis combining X-ray microtomography and pull-out tests. *J Rheology*. 2012;56(3):593–623.
38. Switzer III LH, Klingenberg DJ. Rheology of sheared flexible fiber suspensions via fiber-level simulations. *J Rheology*. 2003;47(3):759–778.
39. Yamanoi M, Leer C, van Hattum FWJ, Carneiro OS, Maia JM. Direct fibre simulation of carbon nanofibres suspensions in a Newtonian fluid under simple shear. *J Colloid Interface Sci*. 2010;347(2): 183–191.
40. Kim S, Karrila SJ. Microdynamics: Principles and Selected Applications. Boston, MS: Butterworth - Heinemann; 1991.
41. Souloumiac B, Vincent M. Steady shear viscosity of short fibre suspensions in thermoplastics. *Rheologica Acta*. 1998;37(3):289–298.
42. Gibson AG, Toll S. Mechanics of the squeeze flow of planar fibre suspensions. *J Non-Newtonian Fluid Mech*. 1999;82:1–24.
43. Doi M, Edwards SF. Dynamics of rod-like macromolecules in concentrated solution. Part 1. *J Chem So, Faraday Trans 2*. 1978;74: 560–570.
44. Bird RB, Curtiss CF, Armstrong RC, Hassager O. Dynamics of Polymeric Liquids. Vol. 2, Kinetic Theory. 2nd ed. New York: Wiley; 1987.
45. Doi M, Edwards SF. The Theory of Polymer Dynamics. New York, NY: Oxford University Press; 1986.
46. Advani SG, Tucker III CL. Closure approximations for three-dimensional structure tensors. *J Rheology*. 1990;34(3):367–386.
47. Cintra JS, Tucker III CL. Orthotropic closure approximations for flow-induced fiber orientation. *J Rheology*. 1995;39(6):1095–1122.
48. Chung DH, Kwon TH. Improved model of orthotropic closure approximation for flow induced fiber orientation. *Polym Compos*. 2001;22(5):636–649.
49. Férec J, Heniche M, Heuzey MC, Ausias G, Carreau PJ. Numerical solution of the Fokker-Planck equation for fiber suspensions: Application to the Folgar-Tucker-Lipscomb model. *J Non-Newtonian Fluid Mech*. 2008;155(1–2):20–29.
50. Sepehr M, Ausias G, Carreau PJ. Rheological properties of short fiber filled polypropylene in transient shear flow. *J Non-Newtonian Fluid Mech*. 2004;123(1):19–32.
51. Carreau PJ, De Kee D, Chhabra RP. Rheology of Polymeric Systems: Principles and Applications. Munich, Germany: Hanser; 1997.
52. Goto S, Nagazono H, Kato H. The flow behavior of fiber suspensions in Newtonian fluids and polymer solutions. *Rheologica Acta*. 1986;25(3):246–256.
53. Ammar A, Mokdad B, Chinesta F, Keunings R. A new family of solvers for some classes of multidimensional partial differential equations encountered in kinetic theory modeling of complex fluids. *J Non-Newtonian Fluid Mech*. 2006;139(3):153–176.
54. Ammar A, Mokdad B, Chinesta F, Keunings R. A new family of solvers for some classes of multidimensional partial differential equations encountered in kinetic theory modelling of complex fluids: Part II: Transient simulation using space-time separated representations. *J Non-Newtonian Fluid Mech*. 2007;144(2–3):98–121.

Manuscript received Sept. 16, 2013, and revision received Nov. 29, 2013.